Original Research Article

International journal of spray and combustion dynamics

International Journal of Spray and Combustion Dynamics
2017, Vol. 9(4) 394–408

DOI: 10.1177/1756827717703576
journals.sagepub.com/home/scd
SAGE

Shape optimization of a Helmholtz resonator using an adjoint method

Faisal Caeiro, Carlo Sovardi, Kilian Förner and Wolfgang Polifke

Abstract

This paper proposes a method for shape optimization in aero-acoustics and applies it to a Helmholtz resonator. The objective is to realize a desired acoustic impedance by optimizing the shape of the neck of the resonator, in due consideration of the excitation level. The optimization problem is formulated with a suitable objective functional, where the Navier–Stokes equations act as a partial differential equation (PDE) constraint in a Lagrangian functional. By exploiting the understanding of the relevant flow physics, it is possible to formulate the objective functional in the time domain, although the optimization target, i.e. the acoustic impedance, is a quantity defined in the frequency domain. This optimization problem is solved by a gradient-based optimization. The shape gradient of the objective functional is determined by an adjoint method, which requires solving two sets of PDEs in time: the so-called forward and backward problems. The forward problem is represented by the Navier–Stokes equations and is solved in the positive time direction. The set of equations for the backward problem, which has to be solved in the negative time direction, is derived in the current study. From the solutions of the forward and backward problems, the shape derivative for the current optimization step is calculated. Iterative optimization steps then bring the impedance to the target value.

Keywords

Unsteady shape optimization, Lagrangian PDE-constrained optimization, backward stepping adjoint, Helmholtz resonator, nonlinear acoustics

Date received: 31 August 2016; accepted: 13 March 2017

1. Introduction

Helmholtz resonators, perforated liners, or quarter wave cavities are different types of acoustic resonators used in combustion systems such as rocket combustion chambers, aero-engines, or gas turbines.[1] Their purpose is to increase dissipation of acoustic energy, thus controlling thermo-acoustic combustion instabilities or reducing emissions of noise. They are usually passive devices and some tuning for a good performance at the expected working conditions is required.

In the past decade, algorithm-based shape, topology, and form optimization have become powerful tools for expediting the design phase in engineering. A design boundary whose properties are quite good by engineering design, but not ideal, can be modified iteratively through a process called shape optimization. Classical optimization methods used widely today are the Hadamard method for geometric optimization,[2,3] homogenization methods for topology optimization,[4,5] and variational techniques with Sobolev smoothing.[6] Shape optimization is applied to structural, vibrational, aerodynamic, and acoustic problems.

In recent years, acoustic optimization, in particular, has become a major area of research with applications in the fields of structural-acoustic optimization and aero-acoustic optimization. In aero-acoustic optimization, the shape of reactive mufflers was optimized using transmission matrix technique. Bernhard developed a semi-analytic sensitivity analysis formulation.[7] For gradient-based shape optimization of a sound barrier,

Fakultät Maschinenwesen, Technische Universität München, Garching, Germany

Corresponding author:
Kilian Förner, Fakultät Maschinenwesen, Technische Universität München, Boltzmannstr. 15, D-85747 Garching, Germany.
Email: foerner@tfd.mw.tum.de

Habbal used a finite element method (FEM) to solve the linear acoustic problem and an adjoint equation to compute the shape sensitivity.[8] Christensen and Olhoff applied a boundary element method to optimize the directivity pattern of a loudspeaker diaphragm by variation of ring mass distribution and geometry.[9] Bängtsson et al. optimized with a gradient scheme the shape of an acoustic horn in order to minimize reflections in the waveguide,[10] while matching the impedance of the surrounding fluid.

In the present paper, the shape of the neck of an acoustic resonator is optimized to match the resonator impedance with that of the surrounding fluid. A gradient-based optimization technique (method of steepest descent) is used, which requires accurate calculation of shape derivatives. For this purpose, the method introduced by Céa is adopted,[11] which derives an adjoint equation from a Lagrangian functional comprising the objective functional. The partial differential equation (PDE) of the forward problem is introduced as a constraint in the Lagrangian functional. Shape sensitivity is calculated from the solutions of the forward problem and the adjoint equation.

To numerically determine the orifice transfer impedance through the neck, a segregated approach is adopted.[12,13] The unsteady Navier–Stokes equations are considered to simulate the fluctuating fluid flow and thus represent the forward problem in the present case. Using discrete Fourier transform of the velocity and pressure terms, the impedance is calculated. Since the main objective of a Helmholtz resonator is to induce dissipation of acoustic energy, the shape optimization aims to increase/decrease acoustic dissipation by modifying the boundary at the neck to match the resistive impedance with the specific impedance of surrounding fluid, such that the boundary is fully non-reflecting.

This paper is organized as follows: first working principles and theoretical description of a Helmholtz resonator are discussed. Then the procedure for computing the reactance and resistive parts of the resonator impedance is presented. The unsteady Navier–Stokes problem is introduced for numerical simulations to calculate the impedance. The ingredients for optimization, such as the objective functional, the adjoint equations, and the shape derivative are introduced. Finally, the results are discussed, where the resistive part of the acoustic impedance is optimized to match with the target value of the specific impedance.

2. Acoustic characterization of a Helmholtz resonator

Resonators are often characterized by their acoustic *impedance* Z in the frequency domain. It is defined as the ratio of the Fourier transforms of the fluctuating acoustic pressure $\hat{p}$ and the velocity $\hat{u}$ normal to the reference surface

$$Z(\omega) = z\rho_0 c_0 = \frac{\hat{p}(\omega)}{\hat{u}(\omega)} \tag{1}$$

where ω is the angular frequency. The reference surface at x_{ref} is shown as a dotted line in Figure 1. The impedance, denoted by upper case Z, is often normalized with the *specific impedance* $\rho_0 c_0$, where ρ_0 and c_0 are the mean density and the speed of sound of the mean flow field, respectively. The normalized impedance $Z/\rho_0 c_0$ is denoted by lower case z in the following. The imaginary part of the impedance is referred to as *reactance* and its real part as *resistance*. Assuming one-dimensional (1D) acoustics in front of the resonator, the resonator can be characterized in terms of characteristic wave amplitudes f and g, as sketched in Figure 1. Here, f is the right-traveling wave and g is the left-traveling wave. In the absence of mean flow they are given as

$$f = \tfrac{1}{2}\left(\tfrac{p'}{\rho_0 c_0} + u'\right) \text{ and } g = \tfrac{1}{2}\left(\tfrac{p'}{\rho_0 c_0} - u'\right) \tag{2}$$

The variables p' and u' are fluctuating acoustic pressure and velocity, respectively. The reflection coefficient R is defined as the ratio of the reflected wave $\hat{g}$ to incident wave $\hat{f}$ in the frequency domain. Its relation to the impedance is given as

$$R(\omega) = \frac{\hat{g}}{\hat{f}} = \frac{Z(\omega) - \rho_0 c_0}{Z(\omega) + \rho_0 c_0} = \frac{z(\omega) - 1}{z(\omega) + 1} \tag{3}$$

At the resonator eigenfrequency, the reactance $\Im(Z) = 0$ and the optimal resistance equals the specific impedance $\rho_0 c_0$, i.e. $z = 1$. This implies that no reflections take place ($|R| = 0$). For a resistance larger than this optimal value $\Re(z) > 1$, the resonator is said to be *over-damped*. In this case, the reflection coefficient grows with a further increase of the resistance.

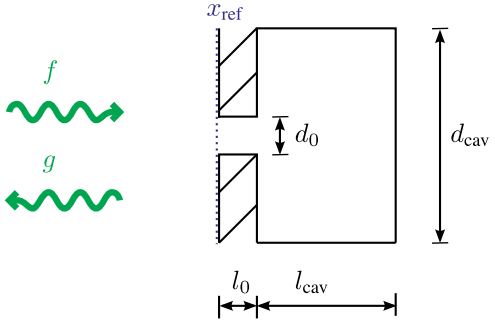

Figure 1. Sketch of a Helmholtz resonator indicating the geometries of neck l_0, d_0 and cavity l_{cav},d_{cav}. Incoming and reflected acoustic waves are indicated by f and g, respectively.

2.1. Segregation of a resonator into neck and cavity

Ingard and Ising suggested that a Helmholtz resonator should be considered as an assembly of two components:[12] the "neck," i.e. the orifice, and the cavity, i.e. the backing volume; see Figure 1. The Helmholtz number He of a Helmholtz resonator, defined as the ratio of neck length l_0 to the acoustic wavelength $\lambda = 2\pi c_0/\omega$, is very small (He $\ll 1$) for the configuration considered. It follows that the orifice is acoustically compact and that the flow through the neck can be treated as incompressible. Effects of compressibility must be taken into account only for the cavity. Tournadre et al. showed that by such segregation,[13] the Helmholtz resonator can be correctly characterized in the nonlinear regime by incompressible computational fluid dynamics (CFD) simulations of the corresponding orifice.

The orifice transfer impedance Z_o may be used to describe the acoustic characteristics of the resonator neck. It is defined as the ratio of the pressure drop $\Delta\hat{p}$ across the orifice (from ① to ② in Figure 2) to the fluctuating velocity in the duct in front of the resonator

$$Z_o = \frac{\Delta\hat{p}}{\hat{u}} \tag{4}$$

The velocity $\hat{u}$ above refers to the cross-sectional average velocity fluctuations in the duct. Note that other authors define the transfer impedance based on the velocity in the orifice. Both definitions are fundamentally equivalent, but differ from each other by a the open area ratio σ, defined as

$$\sigma \equiv \frac{d_0^2}{d_{\text{cav}}^2} \tag{5}$$

Using 1D analysis, the contribution of the orifice can be obtained by subtracting the cavity contribution, such that

$$Z_o = \frac{\hat{p}_1 - Z_{\text{cav}}\,\hat{u}_2}{\hat{u}_1} \tag{6}$$

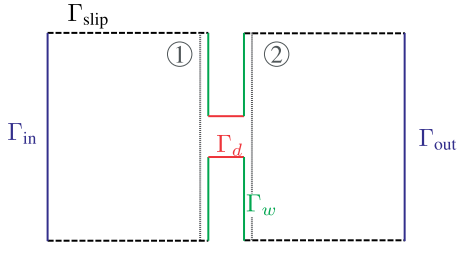

Figure 2. Computational domain and reference planes for the transfer impedance defined in equation (4).

where Z_{cav} is the surface impedance of the backing volume. Since the cross-sectional areas on both sides of the neck are equal, it is reasonable to assume that $\hat{u}_1 = \hat{u}_2$. Thus, the overall surface impedance is given as

$$Z = Z_o + Z_{\text{cav}} \tag{7}$$

In this paper, an incompressible solver is used for simulation of oscillating flow within the orifice including the flow separation at the edges. In general, only the orifice contributes to the resistance of the resonator, i.e. $\Re(Z) = \Re(Z_o)$. The reactance, on the other hand, is influenced by both the orifice and the backing cavity. The resistance of the orifice is always strictly positive. The goal of this paper is to drive the resistance $\Re(Z_o)$ of the resonator to a specific value.

2.2. Linear and nonlinear influences

To understand the relevant flow mechanisms that govern the resonator behavior, the 1D unsteady Bernoulli equation with suitable extensions for the losses is studied.[14,15] The fluctuating pressure drop $\Delta p'$ through the orifice is given as

$$\Delta p' = \underbrace{\rho_0 \frac{l_e}{\sigma}\frac{\partial u'}{\partial t}}_{\text{inertia}} + \underbrace{\frac{1}{2}\rho_0 \frac{u'|u'|}{C_d^2\sigma^2}}_{\text{flow separation}} + \underbrace{R_l u'}_{\text{viscosity}} \tag{8}$$

The first term on the right-hand side (r.h.s.) of equation (8) accounts for the inertia of the fluid in the vicinity of the opening and it represents the reactive part of the orifice transfer impedance. The effective length l_e equals the geometrical length of the orifice l_0 elongated by a length correction, which accounts for the fluid in front of the openings that partakes in the oscillation.[14]

The second term on the r.h.s. represents the effects of flow separation at the edges of the orifice. A jet forms, driven by the acoustic pulsations and eventually dissipated by viscosity, such that it acts as an acoustic loss. The ratio C_d of the cross-sectional area of the jet to the area of the opening is known as the *vena contracta factor* or as the *discharge coefficient*.[16]

The third term on the r.h.s. represents linear thermo-viscous losses at the walls of the orifice, with a real-valued constant R_l. The second and third terms constitute the resistive part of the orifice transfer impedance.

Note that the inertia and the viscous terms depend in a linear fashion on the velocity u'. The flow separation term, on the other hand, behaves nonlinearly with respect to a change in the velocity u', such that the orifice impedance changes with excitation amplitude (unless excitation levels are small).

By increasing the overall viscous dissipation, the resistance $\Re(Z_o)$ is increased and vice versa. This connection will be exploited later while formulating the optimization problem.

3. The computational setup

As explained previously, a segregated approach is used to model the resonator, meaning that only the resonator neck is considered in the numerical computation, while the contribution of the backing volume is modeled analytically. The neck is acoustically compact, thus the numerical computation can be based on the incompressible Navier–Stokes equations. Figure 2 presents schematically the computational domain, including the labeling of the boundaries.

At the inlet boundary Γ_{in} oscillating flow is imposed

$$\boldsymbol{u}_{\text{in}} = A_u \sin(\omega t)\boldsymbol{n} \tag{9}$$

where ω is the angular frequency of the sinusoidal excitation signal. Here and in the following, the vector $\boldsymbol{n}$ denotes a surface normal vector. At the boundary Γ_{out}, an outflow condition is applied. No-slip wall boundary conditions are implemented along the walls of the neck Γ_w and Γ_d, since here viscous dissipation is significant. At the remaining boundaries Γ_{slip} marked with a dashed line in Figure 2, a slip wall boundary condition is appropriate, because resistive losses in the channel and the cavity are negligible.

In summary, the strong form of the Navier–Stokes equations for unsteady, incompressible, viscous flow in domain Ω is given by

$$\begin{aligned}
\tfrac{\partial \boldsymbol{u}}{\partial t} + (\boldsymbol{u}\cdot\nabla)\boldsymbol{u} - \nu\Delta\boldsymbol{u} + \nabla p = 0 \quad & \text{on } \Omega\times(0,T)\\
\nabla\cdot\boldsymbol{u} = 0 \quad & \text{on } \Omega\times(0,T)\\
\boldsymbol{u} = \boldsymbol{u}_{\text{in}} \quad & \text{on } \Gamma_{\text{in}}\times(0,T)\\
\nu\tfrac{\partial \boldsymbol{u}}{\partial n} - p\boldsymbol{n} = 0 \quad & \text{on } \Gamma_{\text{out}}\times(0,T)\\
\boldsymbol{u} = 0 \quad & \text{on } \Gamma_w\cup\Gamma_d\times(0,T)\\
\boldsymbol{u}\cdot\boldsymbol{n} = 0 \quad & \text{on } \Gamma_{\text{slip}}\times(0,T)\\
\boldsymbol{u} = 0 \quad & \text{on } \Omega\times\{0\}
\end{aligned} \tag{10}$$

where $\boldsymbol{u}$ is the velocity vector, ν is the kinematic viscosity of air, and p is the pressure. The boundaries Γ_{in}, Γ_{out}, Γ_{slip}, Γ_w, and Γ_w are sketched in Figure 2. The termination time of the simulation is denoted by T.

As explained in the following, the adjoint method requires solving two PDEs, one for the state variables and one for the so-called adjoint variables. The Navier–Stokes equations presented above are the PDE for the state variables velocity $\boldsymbol{u}$ and pressure p. In an adjoint framework, the PDE for the state variables is referred to as *primal* or *direct problem*.

In the simulations, no turbulence model is applied. Förner et al. showed that for the excitation levels and the geometry considered in the present study including such a model influences the results only insignificantly.[17] The strength of acoustic forcing is usually provided in terms of the sound pressure level (SPL). The SPL is measured in dB as $20\log_{10}(p_{\text{rms}}/20\ \mu\text{Pa})$, where p_{rms} denotes the root mean square of the current pressure fluctuation. The Reynolds number based on the particle velocity in the resonator opening and the size of the opening is low (maximum $\text{Re}\approx 3000$ at 119.7 dB).

The simulations are performed with the FEM using the open source code `FreeFem++`.[18] Linear and quadratic ansatz functions have been used for the velocity and the pressure, respectively. Solving the optimization problem requires solving another PDE, the adjoint problem, as described in the following. In that PDE, the same ansatz functions are applied for the counterpart velocity and the pressure ($\boldsymbol{\lambda}$ and q).

4. Shape optimization

In this section, a procedure for shape optimization is presented. First, a generic shape optimization approach is introduced, based on the derivative of a Lagrangian functional with a PDE system as a constraint. In particular, the approach introduced by Céa is adopted.[11] A general formulation is developed and applied to the unsteady, incompressible Navier–Stokes equations.

The proposed approach addresses acoustic problems. However, in acoustics, it is often appropriate to define the optimization objective in the frequency domain. A frequency domain objective functional cannot be applied to formulate an unsteady problem in a straightforward manner. This gap between the time and frequency domain is closed by exploiting physical knowledge about the problem under investigation, i.e. optimization of the neck of a Helmholtz resonator. Once the objective functional for the Helmholtz resonator case is set up, the corresponding adjoint problem can be formulated. Solving the adjoint system allows calculating the shape derivative, which is required to improve the shape of the neck successively.

4.1. Generic procedure description

The shape optimization problem is introduced in an abstract manner. This section summarizes overall procedure of the computation of the shape derivative based on the Lagrangian method of Céa.[11] The equations that result for the specific resonator case are presented in the

subsequent sections. An extensive derivation of the formalism is given in the Appendix.

Mathematically, the shape optimization problem can be expressed as follows:

Problem 1 *Let* $d \in \{2, 3\}$ *and* $\mathcal{O}_{ad} \subset \{\Omega \subset \mathbb{R}^d \,|\, \Omega \text{ is bounded}\}$ *be a set of admissible domains. Then, the optimization problem is defined as*

$$\min_{\Omega \in \mathcal{O}_{ad}} J(\tilde{\boldsymbol{p}}, \Omega) \text{ with } J = \int_0^T j(\tilde{\boldsymbol{p}}, \Omega)\mathrm{d}t \tag{11}$$

such that $E(\tilde{\boldsymbol{p}}(t), \Omega) = 0 \quad \text{for all } t \in [0, T]$.

$J(\tilde{\boldsymbol{p}}, \Omega)$ is a proper cost function which depends on both domain Ω and *state variable* $\tilde{\boldsymbol{p}}$. The latter is the variable (or the vector of variables) of an unsteady partial differential system of equations $E(\tilde{\boldsymbol{p}}(t), \Omega) = 0$ defined on the domain Ω. This system of PDEs is referred to as *state equations* and represents a constraint for the optimization. By a variation of the computational domain Ω, the solution of the PDE in the given domain, at a given instant t, $\tilde{\boldsymbol{p}}(t, \Omega) = \tilde{\boldsymbol{p}}_\Omega$ will change. The value of the objective functional used for the optimization (which depends on $\tilde{\boldsymbol{p}}(t, \Omega) = \tilde{\boldsymbol{p}}_\Omega$ will be affected accordingly.

The goal of a generic unsteady shape optimization is to find an optimal domain Ω such that an objective functional $J(\tilde{\boldsymbol{p}}, \Omega)$ is minimized. In the present work, a gradient-based, iterative method is applied to solve the problem. At each step of the optimization process, a deformation $\boldsymbol{\theta}$ of the current domain Ω_0 is performed, as sketched schematically in Figure 3. It moves every point $\boldsymbol{x}_0$ in the domain to another point in space $(\mathrm{Id} + \boldsymbol{\theta})(\boldsymbol{x}_0) = \boldsymbol{x}_0 + \boldsymbol{\theta}(\boldsymbol{x}_0)$. Here, Id denotes the identity operator and $\boldsymbol{\theta}(\boldsymbol{x}_0)$ is the shift vector of the point $\boldsymbol{x}_0$.

The deformation $\boldsymbol{\theta}$ is computed by means of the so-called shape derivative. The shape derivative $J'(\Omega)$ describes how the objective functional $J(\Omega)$ changes as a result of displacement of any point on the boundary $\Gamma = \partial\Omega$. The Taylor expansion around the reference domain Ω_0 with respect to a deformation $\boldsymbol{\theta}$ can be written as follows

$$J((\mathrm{Id} + \boldsymbol{\theta})(\Omega)) = J(\Omega) + J'(\Omega)(\boldsymbol{\theta}) + o(\boldsymbol{\theta}) \tag{12}$$

Accordingly, the objective functional decreases (for a small enough step size) if a deformation $\boldsymbol{\theta}$ such that $J'(\Omega)(\boldsymbol{\theta}) < 0$ is applied.

In this work, the shape derivative is computed using the Lagrangian method since the cost function depends on the solution of the system of PDEs represented by the Navier–Stokes equations. The Lagrangian functional $\mathcal{L}$ is constructed by adding the variational formulation of the PDE system as a constraint to the objective functional. Mathematically, this is written as follows

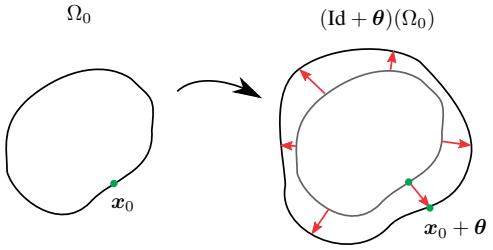

Figure 3. Transformation of a generic domain Ω_0 with $\mathrm{Id} + \mathrm{I}\theta$.

$$\begin{aligned} \mathcal{L}(\Omega; \tilde{\boldsymbol{q}}, \tilde{\boldsymbol{p}}) &= \int_0^T l(\Omega, \tilde{\boldsymbol{q}}, \tilde{\boldsymbol{p}})\mathrm{d}t \\ \text{with } l &= \underbrace{j(\Omega; \tilde{\boldsymbol{p}})}_{\text{Cost function}} + \underbrace{a(\Omega; \tilde{\boldsymbol{q}}, \tilde{\boldsymbol{p}}) - f(\Omega; \tilde{\boldsymbol{q}})}_{\text{Variational form state equations}} \end{aligned} \tag{13}$$

where $\tilde{\boldsymbol{q}}$ is the Lagrangian multiplier that enforces the fulfillment of the PDE constraint in weak form. Equivalently $\tilde{\boldsymbol{q}}$ can be interpreted as the test function of the PDE system of equations in weak form: $a(\Omega; \tilde{\boldsymbol{q}}, \tilde{\boldsymbol{p}}) - f(\Omega; \tilde{\boldsymbol{q}}) = 0$.

The stationarity of $\mathcal{L}(\Omega; \tilde{\boldsymbol{q}}, \tilde{\boldsymbol{p}})$ which gives the minimum of equation (13) is found where its gradient is null. This implies the computations of the partial derivatives of the Lagrangian function with respect to (w.r.t.) each variable. Following Céa at first principles,[11] the variables $\tilde{\boldsymbol{q}}, \tilde{\boldsymbol{p}}$ in the Lagrangian equation (13) do not depend on Ω but belong to a proper functional space of $\mathbb{R}^d$. Consequently, it is possible to compute the partial derivative of each variable with the usual partial differentiation.

The partial derivative of Lagrangian functional with respect to $\tilde{\boldsymbol{q}}$ evaluated in the direction of the function $\boldsymbol{\psi}$ returns the forward problem/state equation (or primal problem) in the variational form

$$\left\langle \frac{\partial}{\partial \tilde{\boldsymbol{q}}} l(\Omega; \tilde{\boldsymbol{q}}, \tilde{\boldsymbol{p}}); \boldsymbol{\psi} \right\rangle = \int_0^T [a(\Omega; \boldsymbol{\psi}, \tilde{\boldsymbol{p}}) - f(\Omega; \boldsymbol{\psi})]\mathrm{d}t = 0 \tag{14}$$

which is null for $\tilde{\boldsymbol{p}} = \tilde{\boldsymbol{p}}_\Omega$ solution of the state equation in the domain Ω (which depends on the shape of the domain Ω). Here, $\langle ., . \rangle$ is the scalar product for vector valued functions, i.e. $\langle \boldsymbol{f}_1, \boldsymbol{f}_2 \rangle = \int_0^T \int_\Omega \boldsymbol{f}_1(\boldsymbol{x}) \cdot \boldsymbol{f}_2(\boldsymbol{x})\mathrm{d}V\mathrm{d}t$ or $\langle \boldsymbol{f}_1, \boldsymbol{f}_2 \rangle = \sum_{i=1}^n \int_0^T \int_\Omega f_{1,i}(\boldsymbol{x}) f_{2,i}(\boldsymbol{x})\mathrm{d}V\mathrm{d}t$.

The partial derivative of Lagrangian functional with respect to $\tilde{\boldsymbol{p}}$ evaluated in the direction of the function $\boldsymbol{\varphi}$

and for $\tilde{\boldsymbol{p}} = \tilde{\boldsymbol{p}}_\Omega$ defines the adjoint equation

$$\left\langle \frac{\partial}{\partial \tilde{\boldsymbol{p}}} \mathcal{L}(\Omega; \tilde{\boldsymbol{q}}, \tilde{\boldsymbol{p}}_\Omega); \boldsymbol{\varphi} \right\rangle = \int_0^T [j'(\Omega, \tilde{\boldsymbol{p}}_\Omega, \boldsymbol{\varphi}) + a(\Omega; \tilde{\boldsymbol{q}}, \boldsymbol{\varphi})] \mathrm{d}t = 0 \tag{15}$$

which is null for $\tilde{\boldsymbol{q}} = \tilde{\boldsymbol{q}}_\Omega$ solution of the adjoint equation in the domain Ω (which depends on the shape of the domain Ω). It can be seen that the adjoint equation depends on the choice of the object function. Moreover, it depends also on the solution of the primal problem equation (14) $\tilde{\boldsymbol{p}}_\Omega$ in the domain Ω, which thus has to be solved first.

For a given domain Ω at the stationary point $(\tilde{\boldsymbol{p}}_\Omega, \tilde{\boldsymbol{q}}_\Omega)$ at which both partial derivatives w.r.t. the variables $\tilde{\boldsymbol{p}}$ and $\tilde{\boldsymbol{q}}$ are null, one can define the shape derivative as follows

$$\begin{aligned} &\frac{\mathrm{d}}{\mathrm{d}\Omega} \mathcal{L}(\Omega; \tilde{\boldsymbol{q}}_\Omega, \tilde{\boldsymbol{p}}_\Omega)(\boldsymbol{\theta}) \\ &= \frac{\partial}{\partial \Omega} \mathcal{L}(\Omega; \tilde{\boldsymbol{q}}_\Omega, \tilde{\boldsymbol{p}}_\Omega)(\boldsymbol{\theta}) + \left\langle \frac{\partial}{\partial \tilde{\boldsymbol{q}}} l(\Omega; \tilde{\boldsymbol{q}}_\Omega, \tilde{\boldsymbol{p}}_\Omega); \tilde{\boldsymbol{q}}'_\Omega(\Omega)(\boldsymbol{\theta}) \right\rangle \\ &\quad + \left\langle \frac{\partial}{\partial \tilde{\boldsymbol{p}}} l(\Omega; \tilde{\boldsymbol{q}}_\Omega, \tilde{\boldsymbol{p}}_\Omega); \tilde{\boldsymbol{p}}'_\Omega(\Omega)(\boldsymbol{\theta}) \right\rangle \end{aligned} \tag{16}$$

but the second and the third term of equation (16) are null for equations (14) and (15). Consequently, having computed once the solutions $\tilde{\boldsymbol{p}}_\Omega$ and $\tilde{\boldsymbol{q}}_\Omega$ from equations (14) and (15), equation (16), the shape sensitivity, reduces to

$$J'(\Omega, \tilde{\boldsymbol{p}})(\boldsymbol{\theta}) = \frac{\partial}{\partial \Omega} \mathcal{L}(\Omega; \tilde{\boldsymbol{q}}, \tilde{\boldsymbol{p}})(\boldsymbol{\theta}) \tag{17}$$

The Hadamard shape derivatives give the expression for $\boldsymbol{\theta}$ on the boundary to be optimized. Regularization is applied to the gradient before performing mesh morphing. The reason for that is that the optimized solutions to fluid mechanics and acoustic problems often lead to curvy shape solutions. These are often not admissible in engineering application. Hence, the shape gradient needs to be regularized in order to obtained smooth shapes. More details on the shape derivative and the mesh smoothing are given in the Appendix.

For the current optimization problem, the objective functional, the forward, and adjoint problem have to be set up. This is done in the following sections for the Helmholtz resonator.

4.2. Objective functional for Helmholtz resonator problem

The task is to find a resonator neck shape Γ_d that realizes a specific target impedance z_{target} for a given excitation level. The first step in the optimization procedure is to the set the objective functional, which is done for the resonator in this section. Considering an unsteady state equation, the objective functional also has to be defined in in time domain. However, it is often useful in acoustics to define a criterion in the frequency domain, which cannot be used in a straightforward manner. An elegant method to overcome this problem is introduced here.

If the resonator impedance matches the impedance of the surrounding fluid, no reflections take place at the resonator for a normally incident acoustic wave; see equation (3). At the resonator eigenfrequency the reactance vanishes, thus only the resistance is considered in the optimization. However, the reactance is also influenced by the shape of the resonator neck. This results in a slight shift in the resonator eigenfrequency, which may be compensated by a variation of the backing volume; see equation (7). The goal of this study is to achieve a normalized resistance of unity, i.e. $\Re(z_{\text{target}}) = 1$. The proposed procedure is also capable of dealing with arbitrary target resistance values $\Re(z_{\text{target}})$. Note that the optimization is performed for a specific SPL, because the resistance depends on the SPL. Overall, the optimization problem can be formulated as follows

$$\min_{\Omega \in \mathcal{O}_{ad}} \left| \Re(z_{\text{target}}) - \Re(z) \right| \tag{18}$$

The criterion above is not directly applicable, since it is defined in the frequency domain, which makes it unsuitable as an objective functional with the unsteady Navier–Stokes equations as state equations. The proposed procedure aims to bridge the gap between the time and frequency domain perspective to enable shape optimization with respect to the impedance in the nonlinear regime.

For that purpose, the link between the resistance $\Re(z)$ and viscous dissipation is exploited. The dissipation of energy is given as $2\nu S : S$, where S denotes the strain rate tensor $S = 1/2(\nabla \boldsymbol{u} + \nabla \boldsymbol{u}^T)$. An objective functional J to minimize the dissipation can be given as follows

$$J(\Omega, \boldsymbol{u}) = \int_0^T \int_\Omega \frac{\nu}{2} |\nabla \boldsymbol{u}|^2 \mathrm{d}V \mathrm{d}t \tag{19}$$

Note that this objective functional is not totally equivalent to the integrated viscous dissipation but works well in many practical applications.[19] The deformation $\boldsymbol{\theta}$ obtained by using the objective functional in equation (19) is successively scaled by the gradient of objective functional for $\Re(Z)$ defined in equation (18)

$$\widetilde{\boldsymbol{\theta}} = \alpha(\Re(z_{\text{target}}) - \Re(z))\boldsymbol{\theta} \tag{20}$$

where α is a positive number which acts as scaling factor. The mesh extension problem is solved with this scaled deformation vector $\widetilde{\boldsymbol{\theta}}$ and the mesh is morphed finally. Applying this scaling, the viscous dissipation is increased if the current resistance is below the target resistance $\Re(z_{\text{target}})$, and vice versa. Moreover, it acts as an adaptive step size control: If the current resistance is far off the target resistance $\Re(z_{\text{target}})$ a large step is performed, while the step size is reduced when the current resistance is in the vicinity of the target value.

4.3. Adjoint equation for Helmholtz resonator problem

Now, a Lagrangian functional is introduced for the minimization problem of the objective functional with the Navier–Stokes equations as constraints. The velocity $\boldsymbol{u}$ and the pressure form the state variable $\tilde{\boldsymbol{p}} = (\boldsymbol{u}, p)^T$. Here, $\boldsymbol{\lambda}$ is the Lagrangian multiplier (or the test function) for the momentum equations and q is the Lagrangian multiplier (or the test function) for the continuity equation, i.e. $\tilde{\boldsymbol{q}} = (\boldsymbol{\lambda}, q)^T$

$$\begin{aligned}\mathcal{L}(\Omega; \boldsymbol{\lambda}, q, \boldsymbol{u}, p) = &\int_0^T \int_\Omega \frac{\nu}{2}|\nabla \boldsymbol{u}|^2 \mathrm{d}V\mathrm{d}t \\ &+ \int_0^T \int_\Omega \Big[-\frac{\partial \boldsymbol{u}}{\partial t} \cdot \boldsymbol{\lambda} - (\boldsymbol{u} \cdot \nabla)\boldsymbol{u} \cdot \boldsymbol{\lambda} - \nu \nabla \boldsymbol{u} : \nabla \boldsymbol{\lambda} \\ &+ p(\nabla \cdot \boldsymbol{\lambda}) + (\nabla \cdot \boldsymbol{u})q \Big] \mathrm{d}V\mathrm{d}t \end{aligned} \tag{21}$$

Given the solution of the forward problem, the state variables $\boldsymbol{u}, p$ in the domain Ω are known. Here the subscript Ω used in equation (14) to indicate the solution of the primal problem in the domain Ω is omitted to simplify the notation. From the solutions of the state equations $\boldsymbol{u}, p$, the adjoint equation can be derived as presented in the Appendix. The strong form of the adjoint equation is given as

$$\begin{aligned} -\frac{\partial \boldsymbol{\lambda}}{\partial t} - (\boldsymbol{u} \cdot \nabla)\boldsymbol{\lambda} & \\ + (\nabla \boldsymbol{u}) \cdot \boldsymbol{\lambda} - \nu \Delta \boldsymbol{\lambda} + \nabla q = -\nu \Delta \boldsymbol{u} & \quad \text{on } \Omega \times (0, T) \\ \nabla \cdot \boldsymbol{\lambda} = 0 & \quad \text{on } \Omega \times (0, T) \\ \boldsymbol{\lambda} = 0 & \quad \text{on } \Gamma_w \cup \Gamma_d \times (0, T) \\ \boldsymbol{\lambda} = 0 & \quad \text{on } \Gamma_{\text{in}} \times (0, T) \\ \nu \tfrac{\partial \boldsymbol{\lambda}}{\partial \boldsymbol{n}} - q \cdot \boldsymbol{n} = \nu \tfrac{\partial \boldsymbol{u}}{\partial \boldsymbol{n}} & \quad \text{on } \Gamma_{\text{out}} \times (0, T) \\ \boldsymbol{\lambda} \cdot \boldsymbol{n} = 0 & \quad \text{on } \Gamma_{\text{slip}} \times (0, T) \\ \boldsymbol{\lambda} = 0 & \quad \text{on } \Omega \times \{T\} \end{aligned} \tag{22}$$

Since there are no initial conditions for $t = 0$ given but only terminal conditions for $t = T$, this equation has to be solved in reversed time from T to 0 by the so-called *backward stepping*. Correspondingly, the primal and the adjoint equations are also referred to as forward and backward problem, since they are solved forward and backward in time, respectively. This backward stepping requires that the entire solution trajectory of forward problem has to be available during the backward stepping of the adjoint. Specifically, for backward iteration $0, 1, \ldots, n$ the state variable $\boldsymbol{u}^n, \boldsymbol{u}^{n-1}, \ldots, \boldsymbol{u}^0$ are required, likewise p. This presents an algorithmic challenge during implementation of the unsteady adjoint. There are mainly two approaches towards backwards stepping adjoint algorithms, i.e. the *storage method* and the *check-pointing algorithm*.[20–24] Check-pointing algorithm attempts to strike a balance between the spatial/memory requirements and the temporal requirements for re-computation. Since here only two-dimensional (2D) grids are considered for the optimization for a moderate amount of time steps, the storage method is an obvious choice because of its simplicity.

There has been considerable work on backward time stepping over the last decade including commercial optimization codes such as the `doln-adjoint`. The properties of the adjoint mainly the *reverse propagation* and backward stepping are well explained in the software documentation.[20,25,26]

Since the backward problem starts from time T, a *terminal boundary condition* is needed for $\boldsymbol{\lambda}$, which is zero in our case. A more detailed description on the derivation of the adjoint equation is available in the Appendix.

4.4. Shape derivative for Helmholtz resonator problem

The shape derivative for the Lagrangian formulation can be formulated using the standard Hadamard shape derivatives.[27] To evaluate it, first the primal and adjoint problem have to be solved for the state and adjoint variables, respectively. For the unsteady Navier–Stokes equations with the objective functional from equation (19), the shape derivative is given as

$$\begin{aligned}\left\langle \frac{\partial \mathcal{L}}{\partial \Omega}, \boldsymbol{\theta} \right\rangle = J'(\Omega; \boldsymbol{u}, p)(\boldsymbol{\theta}) = \int_0^T \int_{\Gamma_d} \Big[&\frac{\nu}{2}|\nabla \boldsymbol{u}|^2 \\ &+ \frac{\partial \boldsymbol{u}}{\partial t} \cdot \boldsymbol{\lambda} + (\boldsymbol{u} \cdot \nabla)\boldsymbol{u} \cdot \boldsymbol{\lambda} + \nu \nabla \boldsymbol{u} : \nabla \boldsymbol{\lambda} \\ &- p(\nabla \cdot \boldsymbol{\lambda}) + (\nabla \cdot \boldsymbol{u})q \Big] (\boldsymbol{\theta} \cdot \boldsymbol{n}) \mathrm{d}S\mathrm{d}t \end{aligned} \tag{23}$$

By using the boundary conditions on Γ_d, $\boldsymbol{u} = 0$ and $\boldsymbol{\lambda} = 0$, and by canceling out the terms representing continuity equation, the final expression for

shape derivative for the considered problem can be written as

$$J'(\Omega;\boldsymbol{u},p)(\boldsymbol{\theta})=\int_0^T\int_{\Gamma_d}\left[\frac{\nu}{2}|\nabla\boldsymbol{u}|^2+\nu\nabla\boldsymbol{u}:\nabla\boldsymbol{\lambda}\right](\boldsymbol{\theta}\cdot\boldsymbol{n})\mathrm{d}S\mathrm{d}t \tag{24}$$

With the expression above, the sensitivity of the objective functional to the displacement of any point on the boundary can be evaluated. Following the theorem of Hadamard (see Appendix), the deformation for all $\boldsymbol{x}$ on the free boundary Γ_d can be set as

$$\boldsymbol{\theta}(\boldsymbol{x})=-\left(\frac{\nu}{2}|\nabla\boldsymbol{u}(\boldsymbol{x})|^2+\nu\nabla\boldsymbol{u}(\boldsymbol{x}):\nabla\boldsymbol{\lambda}(\boldsymbol{x})\right)\boldsymbol{n}(\boldsymbol{x}) \tag{25}$$

As described in the Appendix, the deformation on the boundary is regularized in order to smoothen it. Successively, the deformation for the entire mesh is calculated.

4.5. Optimization algorithm

Having all ingredients required for the optimization process, the overall algorithm is summarized in this section. A flowchart is shown in Figure 4. The procedure starts with an initial shape Ω_0, which is iteratively improved. This iteration terminates when the difference of the normalized resistance to the target value $|\Re(z_{\text{target}})-\Re(z)|$ is below a tolerance threshold 10^{-5}. If the procedure does not converge, it is stopped when the maximal number of iterations $k_{\max}$ is reached. In each iteration step, the primal problem is solved first. This means that the unsteady Navier–Stokes equation (10) is solved for an excitation with angular frequency ω over three periods $6\pi/\omega$. From the time series, the resistance is calculated via discrete Fourier transform. The adjoint problem of equation (22) is solved successively. The shape derivative on the boundary is evaluated using the state and the adjoint variables. The derivative is regularized (see equation (32) in the Appendix). Based on the current impedance z, the deformation is scaled, see equation (20). The total computational mesh is deformed accordingly, see equation (33). Details on this mesh extension are given in the Appendix. This procedure is repeated until the termination criterion described above applies.

5. Simulation results

In this section, the results obtained from the numerical simulations are discussed. First, the code solving the unsteady Navier–Stokes equations is validated for a three-dimensional (3D) case against numerical results of Tournadre et al. and analytical results.[13] Then, an optimization for a target resistance of unity is performed for two scenarios with different SPLs on a 2D mesh.

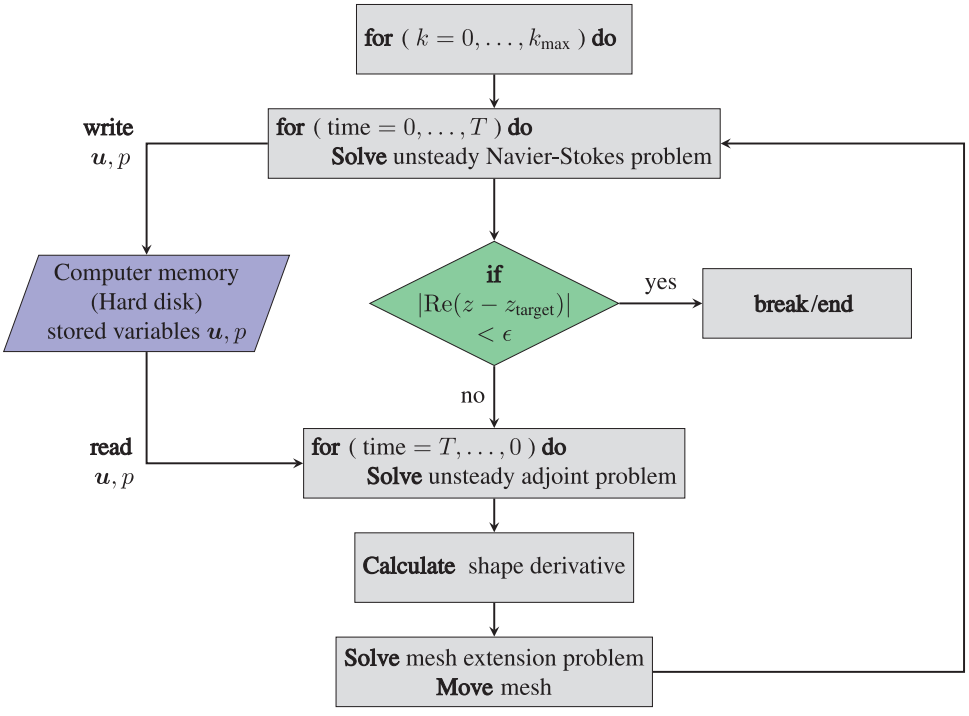

Figure 4. Flowchart describing the algorithm for backward stepping Navier–Stokes equations. In this work, $\epsilon = 10^{-5}$.

5.1. Validation case geometry and mesh generation

The dimensions of the resonator considered, which are listed in Table 1, are taken from Tournadre et al. to have access to validation data.[13] In the simulations, the orifice is placed in between two duct segments of length $l_{ch} = 50$ mm. The 3D computational domain is discretized with approximately 300,000 unstructured tetrahedral elements using `msh3` and `tetgen` in `FreeFem++`. The mesh has a higher resolution close to the neck and especially at the walls. Small cell sizes are required close to the walls to resolve the high velocity gradients in the Stokes layer.

The input velocity signal u' is directly imposed at the inlet boundary. The pressure p' is monitored on the inlet and the outlet boundary in order to compute $\Delta p'$ and thereby the transfer impedance. Appropriate reactance corrections have to be applied since the pressure is not monitored near the mouth of the orifice. From equation (8), the correction for acoustic impedance can be written as

$$\left(\frac{\Delta p'}{\hat{u}}\right)_{\text{correction}} = \mathrm{i}\rho_0 2 l_{ch}\omega \tag{26}$$

Equation (26) has only an imaginary part and thus accounts for reactive corrections. To check the validity of this correction, a simple channel flow with a sine wave input signal was considered. The length of the channel was 0.1 m and the input signal had a frequency of 300 Hz. From the numerical simulation, the normalized transfer impedance was calculated as $0.0141 + 0.4571\mathrm{i}$. According to the correction formula equation (26), the normalized transfer impedance should be equal to $0.0 + 0.4586\mathrm{i}$. The inertia parts agree nicely. The non-zero resistance determined by numerical simulation is quite small and originates from numerical dissipation.

5.2. Validation of the simulation results for the forward problem

Simulations on the mesh presented in the previous section are performed and their results are compared against results of Tournadre et al. obtained with the CFD software Fluent,[13] as well as against semi-analytical expressions given by Keller and Zauner.[28] For validation in the linear regime, the nonlinear terms in the original equation can be dropped. Moreover, since the contribution of the resonator is disassembled into orifice contributions and backing cavity contributions, the reactance contributions due to backing volume can also be dropped. These simplifications give a semi-analytical expression for impedance in the linear regime

$$Z_o(\omega) = \rho_0\left(1 + \frac{\gamma - 1}{\sqrt{\mathrm{Pr}}}\right)\left(1 + \frac{l_o}{d_o}\right)\sqrt{2\nu\omega} + \mathrm{i}l_e\rho_0\omega(1 + s) \tag{27}$$

The variables Pr and γ denote the Prandtl number and the heat capacity ratio, respectively. For small Stokes number, the boundary layer parameter can be estimated as

$$s = \frac{1}{d_0}\left(1 + \frac{\gamma - 1}{\sqrt{\mathrm{Pr}}}\right)\sqrt{2\nu\omega} \tag{28}$$

For the validation case, an SPL of 89.3 dB is considered, as shown in Table 2. The amplitudes for the velocity perturbation are set as in Tournadre et al.[13]

In Figure 5, the simulation results are compared with the simulation results of Tournadre et al.[13] The values that result from equation (27) are also included. Reasonable agreement between all three results is observed.

5.3. Impedance matching with specific impedance

In this section, the aptitude of the proposed procedure is demonstrated for two test cases. As explained above, the aim is to determine a resonator neck shape that exhibits a normalized target resistance $z_{\text{target}} = 1$ for a given frequency and SPL. The convergence behavior and the flow physics of the initial as well as of the resulting geometries are discussed. Only 2D geometries are used here to minimize the computational cost. Hence, slit resonators are studied. Due to the symmetry of the problem, only the upper half of the geometry is considered in the simulations. The target frequency is chosen as 300 Hz for all cases. The velocity amplitude is set such that the target SPL is reached at the resonator opening for $z = 1$[13]

$$A_u = 10^{\mathrm{SPL}/20}\sqrt{2}\frac{20\mu\mathrm{Pa}}{\rho_0 c_0} \tag{29}$$

Table 1. Geometric dimensions considered for simulating the Helmholtz resonator.

l_o (mm)	d_o (mm)	l_{cav}(mm)	d_{cav}(mm)	l_{ch} (mm)
4.0	4.2	50	50	50

Table 2. Amplitudes A_u for SPL 89.3 dB around the resonator eigenfrequency.[13]

f (Hz)	340	360	380	400	420
A_u (m/s)	0.0021	0.0043	0.0024	0.0014	0.0009

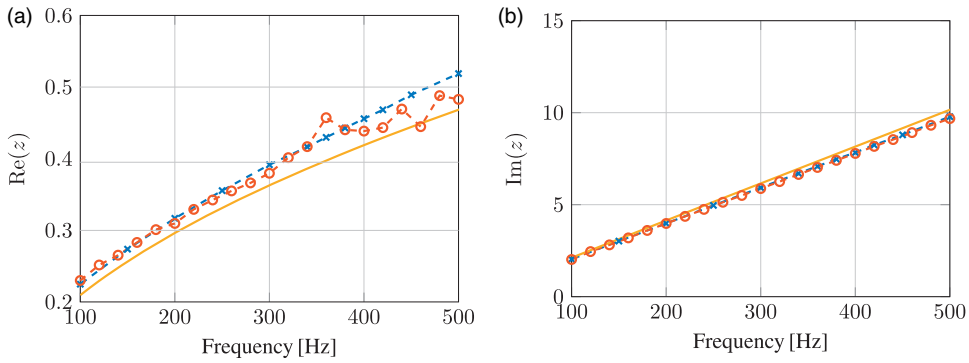

Figure 5. Normalized impedance curves for SPL 89.3 dB obtained from 3D incompressible simulations - *-, Fluent results [13] -o-,[13] and from equation (27) ——. (a) Normalized resistance. (b) Normalized reactance.

The initial slit has the same dimensions l_0 and d_0 as in Table 1. The open area ratio is set to $\sigma_0 = d_0/d_{\text{cav}} = 2\%$. This initial geometry is denoted by Neck0 in the following. In the first case, a SPL of 115 dB is selected. The resulting optimized geometry is referred to as Neck1. In the second test case, the SPL is increased to 120 dB and Neck1 is used as starting neck geometry. The resulting geometry of the optimization in the second test case is named as Neck2. Figure 6 shows the geometries Neck1 (left column), Neck2 (middle), and Neck3 (right) and depicts important flow features of these cases, which will be described and discussed in the following.

The first optimization case is initialized with the geometry Neck0 and a SPL of 115 dB is considered. This mesh consists of 22757 cells. For the forward problem, it exhibits mesh independence with respect to the impedance for both SPLs consider 115 dB and 120 dB. Snapshots during the in- and outflow phases are shown on the left column of Figure 6. In these plots, the respective upper half depicts the flow field with streamlines. The background is colored with respect to the particle velocity amplitude, with red and blue corresponding to high and low velocities, respectively. Each lower half shows the dissipation term $\nu/2|\nabla \boldsymbol{u}|^2$ in a logarithmic scale, as it is used for the definition of the objective functional in equation (19). The same color scheme is applied for all plots. It can be observed that an excitation amplitude of 115 dB already triggers flow separation at the edges of the neck, i.e. it is operated in the nonlinear regime. Here, the flow separates at both the leading and the trailing edge. Dissipation takes mainly place close to the wall, but also in the separation bubbles as shown in the lower halves of the plots.

The change of the normalized resistance with the iteration steps of the optimization k is plotted in Figure 7(a). Here, curves for different scaling factors for the step size α (cf. equation (20)) are included, for $\alpha \in [1, 2.5, 5, 10]$. The initial geometry Neck0 exhibits a normalized resistance 0.343 for the 115 dB excitation. The procedure converges for all values of α to the desired target resistance. However, it can be seen that a larger step, corresponding to a larger value of the scaling factor α, speeds up the convergence significantly. An optimal geometry is detected for $\alpha = 10$ within 22 iterations, while for $\alpha = 1$ the procedure does not reach the target resistance within 400 iterations, which has been set as the maximal number of iterations. The corresponding change in the objective functional J defined in equation (19) is presented in Figure 7(b). Since the initial resistance is too low, the procedure increases the dissipation, which results in the desired increase in the resistance. The flow through the optimized geometry Neck1 is also visualized in Figure 6(a) and (b) in the middle column. It is evident that Neck1 has round edges, which are an outcome of the regularization applied during mesh extension. Round edges tend to reduce the separation effect and thus the nonlinear resistance.[29] Indeed, for Neck1 the flow separates only at a position in the middle of the neck, where the cross-section is narrowest. Simultaneously, the open area ratio is reduced significantly to $\sigma_1 = 0.59\%$. This leads to a considerably higher particle velocity in the neck and thus to more losses. Due to continuity, the average velocity in the neck is increased by a factor of more than three in comparison to the initial configuration. Despite the smooth contour, the velocity is high enough to trigger flow separation. Moreover, the thermo-viscous losses in the boundary layer scale linearly with the velocity and are thus increased considerably. Overall, the in- and decrease of viscous and flow separation losses are balanced in the end in such a way that the desired target impedance is reached.

In the second optimization case, Neck1 is selected as initial geometry but now a higher SPL of 120 dB is considered. As expected, the higher SPL leads to higher particle velocities in the neck; see the center column, Figure 6(c) and (d). The separation bubble is

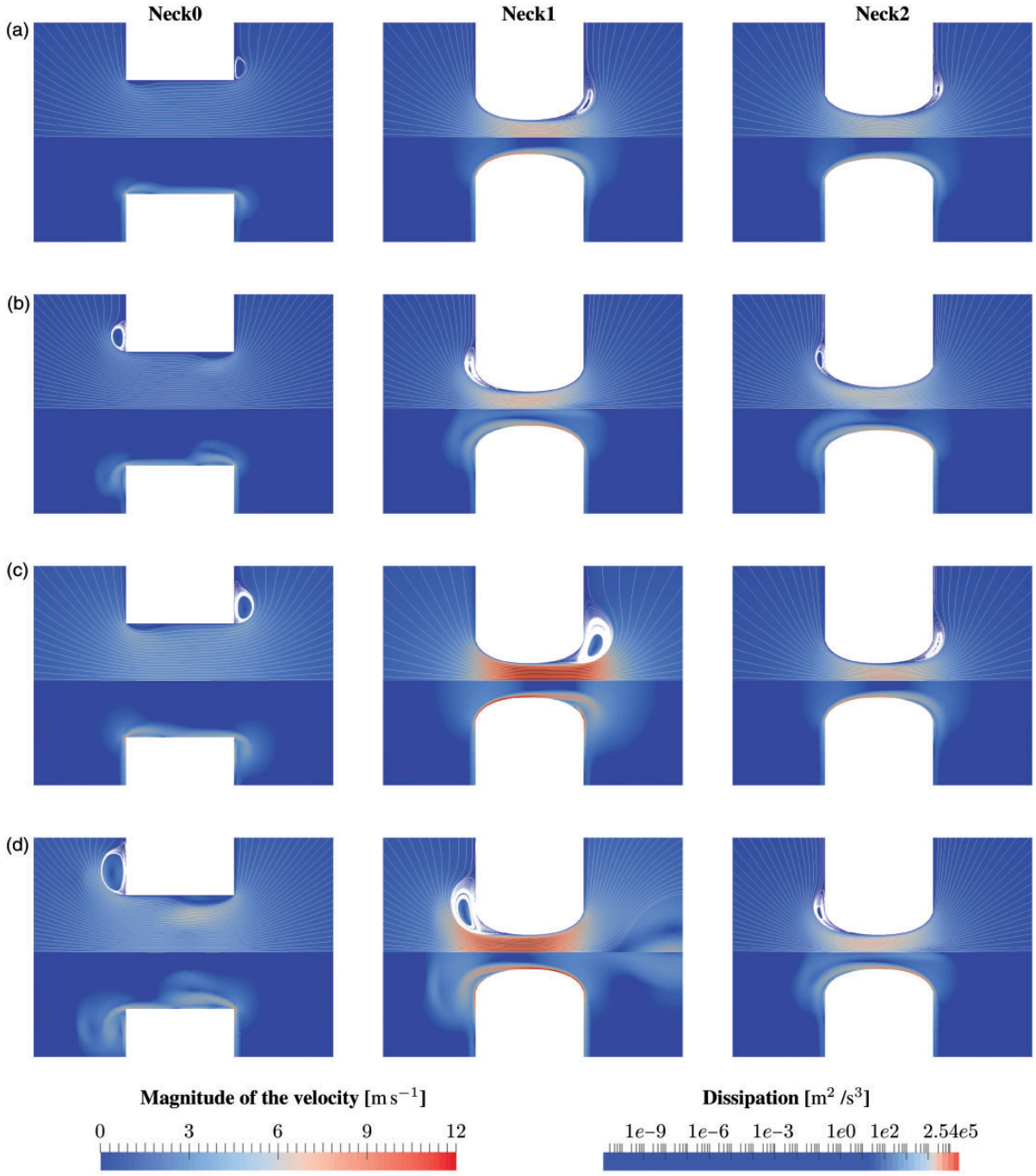

Figure 6. Flow visualization for meshes 1, 2, and 3 at 115 dB and 120 dB during the in- and outflow, respectively. Top: streamlines with background color representing the magnitude of the particle velocity. Bottom: dissipation term $\nu/2|\nabla 1u|^2$. (a) Inflow for 115 dB; (b) outflow for 115 dB; (c) inflow for 120 dB; (d) outflow for 120 dB.

enlarged in comparison to the 115 dB case (cf. Figure 6(a) and (b)). The lower halves of these plots indicate that in the separation zones the dissipation is also increased. This is a nonlinear effect, which leads to a higher resistance in comparison to the 115 dB case. The initial normalized resistance $\Re(z)$ is 1.77 here; see Figure 8(a). The optimization procedure now reduces the viscous losses, as the impedance is too high. Figure 8(b) presents the course of the objective functional defined in equation (19) against the number of iterations k. In Figure 8, only the curves for scaling factors $\alpha \in [1, 2.5]$ are reported, since for higher values $\alpha \in [5, 10]$ the algorithm does not converge. For smaller scaling factors α, the procedure manages

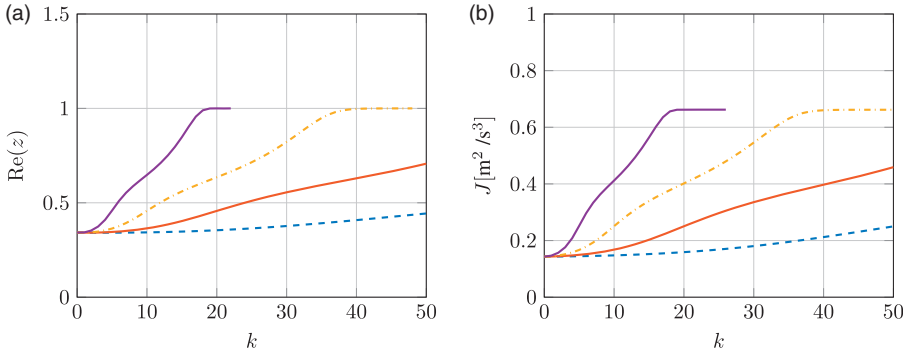

Figure 7. Optimization case 1 with 115 dB. Scaling factor $\alpha = 1$ - - -, $\alpha = 2.5$ ——, $\alpha = 5$ -·-·-, and $\alpha = 10$ ——. (a) Normalized resistance. (b)Objective functional.

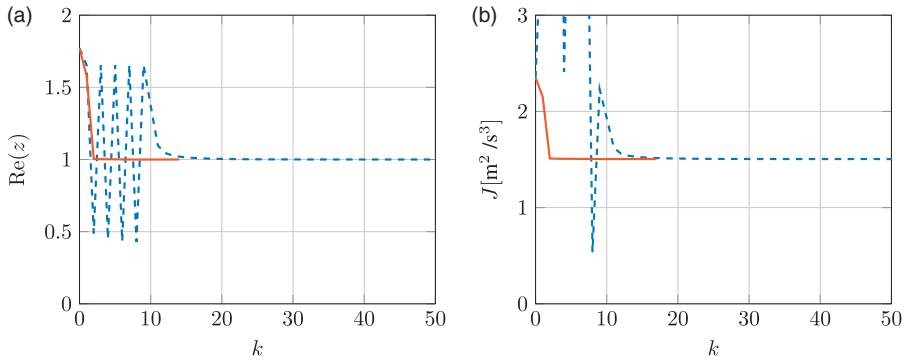

Figure 8. Optimization case 2 with 120 dB. Scaling factor $\alpha = 1$ - - - and $\alpha = 2.5$ ——. (a) Normalized resistance. (b) Objective functional.

to reduce the losses in such a fashion that the target resistance in reached. However, the algorithm also has difficulties for $\alpha = 1$ within the first nine iteration steps but converges finally. The open area ratio of the optimized geometry Neck2 is given as $\sigma_2 = 0.76\%$. This wider open area lowers the velocity in the neck in comparison to Neck1. Thus, the thermo-viscous losses in the boundary layer are reduced. Moreover, the separation bubble shrinks, leading to reduced nonlinear losses.

It can be concluded that the proposed procedure with the coupling of a criterion in the frequency domain and an objective functional in time domain works satisfactorily. The algorithm is capable of changing the geometry such that either a reduction or an increase in the impedance is achieved. The resulting geometries show smooth contours due to the smoothing applied in the mesh extension step. If this is not desired, parametrized geometries could be used instead. Moreover, it can be seen that the convergence behavior is strongly influenced by the scaling factor α. A large factor α can speed up the convergence noticeably, but increases the risk of divergence. Fortunately, this issue can be overcome by using an adaptive step size control.

6. Summary and outlook

An adjoint based method for aero-acoustic shape optimization is introduced. It is applied to optimize a Helmholtz resonator neck, such that a target impedance is reached. The optimization procedure deforms the domain iteratively, making use of the shape derivative, which measures the sensitivity of the objective functional to a local deformation of the domain boundary. For the calculation of the shape derivative, an adjoint approach is used. This requires solving the so-called adjoint equation in addition to the state equation, which describes the physics. The unsteady Navier–Stokes equation serves as state equation, such that nonlinear acoustic effects can also be captured. The impedance is defined in the frequency space and thus cannot serve as an objective functional for a transient problem straightforwardly. This is overcome by choosing the integrated viscous dissipation as objective functional in combination with a step size control. This control ensures that the dissipation is increased when the current impedance is too low and vice versa. The adjoint equation for this setup is derived and the shape derivative is given.

The proposed procedure is applied to two resonator test case with two different excitation levels. In the first case, the initial impedance is below the desired target impedance of unity. The algorithm realizes the target impedance by producing a rounded neck shape with a narrower cross-sectional area which increases the viscous losses at the walls. In the second case, the excitation level is higher. Also here, the algorithm finds a shape with the desired impedance values.

It is expected that the method can be applied to other aero-acoustical applications. It is set up such that it can be used for nonlinear problems for reaching an objective defined in the frequency domain. For larger 3D problems, the memory requirements for the backward stepping represent a bottleneck, which may be overcome by a check-pointing algorithm.

Acknowledgements

This paper is a result of the work completed during work toward the Master's thesis of the first author.[30] A preliminary version of this work was presented at the symposium "Thermoacoustic Instabilities in Gas Turbines and Rocket Engines: Industry meets Academia," Garching, 2016.

Declaration of Conflicting Interests

The author(s) declared no potential conflicts of interest with respect to the research, authorship, and/or publication of this article.

Funding

The author(s) disclosed receipt of the following financial support for the research, authorship, and/or publication of this article: This work was supported by the European Commission via the Marie Curie (ITN) project FlowAirS (project reference 289352) and by the German Research Foundation (Deutsche Forschungsgemeinschaft (DFG)) in the framework of the Sonderforschungsbereich TRR40, Project A3.

References

1. Zhao D and Li XY. A review of acoustic dampers applied to combustion chambers in aerospace industry. *Prog Aerosp Sci* 2015; 74: 114–130.
2. Pironneau O. *Optimal shape design for elliptic systems*. Berlin: Springer-Verlag, 1984.
3. Sokolowski J and Zolesio J-P. *Introduction to shape optimization*. Berlin: Springer, 1992.
4. Allaire G. *Shape Optimization by the homogenization method*. Berlin: Springer, 2001.
5. Bendsoe M and Sigmund O. *Topology optimization: theory, methods and applications*. Berlin: Springer-Verlag, 2003.
6. Jameson A. Aerodynamic shape optimization using the adjoint method. *Lect Von Karman Inst Bruss* 2003. http://aero-comlab.stanford.edu/Papers/jameson.vki03.pdf (accessed 5 May 2017).
7. Bernhard RJ. Shape optimization of reactive mufflers. *Noise Control Eng J* 1986; 27: 10–17.
8. Habbal A. Nonsmooth shape optimization applied to linear acoustics. *SIAM J Optim* 1998; 8: 989–1006.
9. Christensen S and Olhoff N. Shape optimization of a loudspeaker diaphragm with respect to sound directivity properties. *Control Cybern* 1998; 27: 177–198.
10. Bängtsson E, Noreland D and Berggren M. Shape optimization of an acoustic horn. *Comput Methods Appl Mech Eng* 2003; 192: 1533–1571.
11. Céa J. Conception optimale ou identification de formes, calcul rapide de la dérivée directionnelle de la fonction coût. *ESAIM Math Model Numer Anal* 1986; 20: 371–402.
12. Ingard U and Ising H. Acoustic nonlinearity of an orifice. *J Acoust Soc Am* 1967; 42: 6–17.
13. Tournadre J, Förner K, Polifke W, et al. Determination of acoustic impedance for Helmholtz resonators through incompressible unsteady flow simulations. *AIAA J* 2017; 55: 790–798.
14. Ingard U. On the theory and design of acoustic resonators. *J Acoust Soc Am* 1953; 25: 1037–1061.
15. Rienstra SW and Hirschberg A. *An introduction to acoustics*. Technical report no. IWDE 92-06, 2015. Eindhoven, the Netherlands: Eindhoven University of Technology.
16. Cummings A and Eversman W. High amplitude acoustic transmission through duct terminations: theory. *J Sound Vib* 1983; 91: 503–518.
17. Förner K, Tournadre J, Martínez-Lera P, et al. Scattering to higher harmonics for quarter wave and Helmholtz resonators. *AIAA J* 2017; 55: 1194–1204.
18. Hecht F. New development in FreeFem++. *J Numer Math* 2012; 20: 251–265.
19. Ballarin F, Manzoni A, Rozza G, et al. Shape optimization by free-form deformation: existence results and numerical solution for Stokes flows. *J Sci Comput* 2014; 60: 537–563.
20. Griewank A and Walther A. Algorithm 799: Revolve: an implementation of checkpointing for the reverse or adjoint mode of computational differentiation. *ACM Trans Math Softw* 2000; 26: 19–45.
21. Hinze M and Sternberg J. A-Revolve: an adaptive memory-reduced procedure for calculating adjoints with an application to computing adjoints of the instationary Navier–Stokes system. *Optim Methods Softw* 2005; 20: 645–663.
22. Griewank A. Achieving logarithmic growth of temporal and spatial complexity in reverse automatic differentiation. *Optim Methods Softw* 1992; 1: 35–54.
23. Stumm P and Walther A. New algorithms for optimal online checkpointing. *SIAM J Sci Comput* 2010; 32: 836–854.
24. Wang Q, Moin P and Iaccarino G. Minimal repetition dynamic checkpointing algorithm for unsteady adjoint calculation. *SIAM J Sci Comput* 209; 31: 2549–2567.
25. Farrell PE, Ham DA, Funke SW, et al. Automated derivation of the adjoint of high-level transient finite element programs. *SIAM J Sci Comput* 2013; 35: C369–C393.
26. Farrell PE, Funke SW, Ham DA, et al. Dolfin-adjoint 1.6 documentation, http://www.dolfin-adjoint.org/en/latest/documentation/ (2015, accessed 5 May 2017).

27. Hadamard J. Mémoire sur le probléme d'analyse relatif à l'équilibre des plaques élastiques encastrées. *Euvres Jacques Hadamard Mém Sav Étrang* 1968; 33: 515–641.
28. Keller JJ and Zauner E. On the use of Helmholtz resonators as sound attenuators. *Z Angew Math Phys* 1995; 46: 297–327.
29. Förner K, Temiz MA, Polifke W, et al. On the non-linear influence of the edge geometry on vortex shedding in Helmholtz resonators. In: *22nd international congress on sound and vibration (ICSV 22)*, Florence, Italy, 12–16 July 2015. The International Institute of Acoustics and Vibration. http://iiav.org/archives_icsv_last/2015_icsv22/content/papers/papers/full_paper_1341_20150325133515128.pdf.
30. Caeiro F. *Shape optimisation for aeroacoustic optimisation*. Master thesis, TU München, Germany, 2015.
31. Allaire G and Pantz O. Structural optimization with FreeFem++. *Struct Multidiscip Optim* 2006; 32: 173–181.
32. Almgren F and Taylor JE. Optimal geometry in equilibrium and growth. *Fractals* 1995; 3: 713–723.
33. Burger M. A framework for the construction of level set methods for shape optimization and reconstruction. *Interfaces Free Boundaries* 2003; 5: 301–329.
34. Mohammadi B and Pironneau O. *Applied shape optimization for fluids*. Oxford: Clarendon Press, 2001.

Appendix

Shape derivatives

The shape derivative is obtained by the Hadamard structure theorem. From this, the shape derivative is expressed only on the boundary of the shape $\Gamma = \partial\Omega$

$$\langle J'(\Omega), \boldsymbol{\theta} \rangle = \int_\Gamma G(\Omega)(\boldsymbol{\theta} \cdot \boldsymbol{n}) \mathrm{d}S \tag{30}$$

where

$$J(\Omega) = \int_\Omega G(\Omega) \mathrm{d}V \tag{31}$$

Thus, the deformation can be set as $(\boldsymbol{\theta} \cdot \boldsymbol{n}) = -G(\Omega)$. Details of the shape derivative are beyond the scope of this paper and can be found in Allaire and Allaire and Pantz.[4,31]

Gradient smoothing and mesh extension

The regularization of the gradient is written as $\tilde{G} = -(\Delta)^{-1} G$, where G is the defined as in equation (31). The descent direction is then set by the problem

$$\begin{cases} -\Delta \tilde{G} = G & \text{on } \Gamma \\ \tilde{G} = 0 & \text{at end points of } \Gamma \end{cases} \tag{32}$$

For the mesh-morphing of the entire domain and not just the border, the following *extension problem* is introduced

$$\begin{cases} -\Delta \boldsymbol{\theta} = 0 & \text{in } \Omega \\ \frac{\partial \boldsymbol{\theta}}{\partial \boldsymbol{n}} = -\tilde{G}\boldsymbol{n} & \text{on } \Gamma \end{cases} \tag{33}$$

The equation above represents a Neumann-to-Dirichlet map to $-G\boldsymbol{n}$, which has the effect of increasing one order of regularity of $\boldsymbol{\theta}$ on Γ. For further reading refer to Almgren and Taylor,[32] Burger,[33] or Chapter 5 of Mohammadi and Pironneau.[34]

Bängtsson et al. suggest a technique similar to *Tikhonov regularization*,[10] which includes adding a perimeter penalization of the reference boundary Γ_{ref} to the objective functional J. In this paper, gradient regularization refers to the solution of the equation (32).

Adjoint equation

In this section, some details on the derivation of the adjoint equation (22) are shown. The starting point is the Lagrangian defined in equation (21).

The partial derivative of the Lagrangian functional with respect to the adjoint variables reproduces the primal problem equation (10). The partial derivative with respect to $\boldsymbol{\lambda}$ evaluated with the function $\boldsymbol{\psi}$ yields the momentum equation in weak from with $\boldsymbol{\psi}$ as test function

$$\left\langle \frac{\partial}{\partial \boldsymbol{\lambda}} \mathcal{L}(\Omega; \boldsymbol{\lambda}, q, \boldsymbol{u}, p); \boldsymbol{\psi} \right\rangle = \int_0^T \int_\Omega \left[\frac{\partial \boldsymbol{u}}{\partial t} \cdot \boldsymbol{\psi} + (\boldsymbol{u} \cdot \nabla)\boldsymbol{u} \cdot \boldsymbol{\psi} + \nu \nabla \boldsymbol{u} : \nabla \boldsymbol{\psi} - p(\nabla \cdot \boldsymbol{\psi}) \right] \mathrm{d}V \mathrm{d}t = 0 \tag{34}$$

Similarly, the partial derivative with respect to q gives the continuity equation in integrated weak form with r as the test function

$$\left\langle \frac{\partial}{\partial q} \mathcal{L}(\Omega; \boldsymbol{\lambda}, q, \boldsymbol{u}, p); r \right\rangle = \int_0^T \int_\Omega (\nabla \cdot \boldsymbol{u}) r \, \mathrm{d}V \mathrm{d}t = 0 \tag{35}$$

The adjoint equations are derived from the partial derivatives of the Lagrangian functional with respect to the state variables. First, consider the partial derivative with respect to state variable $\boldsymbol{u}$ with the function $\boldsymbol{\varphi}$ which gives

$$\begin{aligned} &\left\langle \frac{\partial}{\partial \boldsymbol{u}} \mathcal{L}(\Omega; \boldsymbol{\lambda}, q, \boldsymbol{u}, p); \boldsymbol{\varphi} \right\rangle \\ &= \int_0^T \int_\Omega \left[\nu \nabla \boldsymbol{u} : \nabla \boldsymbol{\varphi} - \frac{\partial \boldsymbol{\varphi}}{\partial t} \cdot \boldsymbol{\lambda} - (\boldsymbol{\varphi} \cdot \nabla)\boldsymbol{u} \cdot \boldsymbol{\lambda} - (\boldsymbol{u} \cdot \nabla)\boldsymbol{\varphi} \cdot \boldsymbol{\lambda} \right. \\ &\quad \left. - \nu \nabla \boldsymbol{\varphi} : \nabla \boldsymbol{\lambda} + (\nabla \cdot \boldsymbol{\varphi}) q \right] \mathrm{d}V \mathrm{d}t = 0 \end{aligned} \tag{36}$$

The two terms arising from partial derivative of the nonlinear operator have to be written in a slightly different form. Using Gauss theorem yields

$$\int_0^T \int_\Omega (\boldsymbol{u}\cdot\nabla)\boldsymbol{\varphi}\cdot\boldsymbol{\lambda}\mathrm{d}V\mathrm{d}t = -\int_0^T \int_\Omega \boldsymbol{\varphi}\cdot(\boldsymbol{u}\cdot\nabla)\boldsymbol{\lambda}\mathrm{d}V\mathrm{d}t - \int_0^T \int_\Omega \boldsymbol{\varphi}\cdot\boldsymbol{\lambda}(\nabla\cdot\boldsymbol{u})\mathrm{d}V\mathrm{d}t \quad (37)$$

Due to the continuity equation $\nabla\cdot\boldsymbol{u}=0$, the second term in the equation above vanishes. Consider the second term of the nonlinear operator $\int_0^T\int_\Omega(\boldsymbol{\varphi}\cdot\nabla)\boldsymbol{u}\cdot\ \boldsymbol{\lambda}\mathrm{d}V\mathrm{d}t$. It can be rewritten as $\int_0^T\int_\Omega\boldsymbol{\varphi}\cdot(\nabla\boldsymbol{u})\boldsymbol{\lambda}\mathrm{d}V\mathrm{d}t$. Applying Green's first identity and integration over the unsteady term over time gives

$$\begin{aligned}
&-\int_0^T\int_\Omega\left[\nu\Delta\boldsymbol{u}\cdot\boldsymbol{\varphi}\nu\frac{\partial\boldsymbol{u}}{\partial\boldsymbol{n}}\cdot\boldsymbol{\varphi}\right]\mathrm{d}V\mathrm{d}t\\
&+\int_\Omega\Big[\boldsymbol{\varphi}(0)\cdot\boldsymbol{\lambda}(0)-\boldsymbol{\varphi}(T)\cdot\boldsymbol{\lambda}(T)\Big]\mathrm{d}V\\
&+\int_0^T\int_\Omega\left[\frac{\partial\boldsymbol{\lambda}}{\partial t}\cdot\boldsymbol{\varphi}-\boldsymbol{\varphi}\cdot(\nabla\boldsymbol{u})\boldsymbol{\lambda}+\boldsymbol{\varphi}\cdot(\boldsymbol{u}\cdot\nabla)\boldsymbol{\lambda}\right]\mathrm{d}V\mathrm{d}t\\
&+\int_0^T\int_\Omega\nu\Delta\boldsymbol{\lambda}\cdot\boldsymbol{\varphi}\mathrm{d}V\mathrm{d}t-\int_0^T\int_\Gamma\nu\frac{\partial\boldsymbol{\lambda}}{\partial\boldsymbol{n}}\cdot\boldsymbol{\varphi}\mathrm{d}S\mathrm{d}t\\
&-\int_0^T\int_\Omega(\nabla q)\cdot\boldsymbol{\varphi}\mathrm{d}V\mathrm{d}t+\int_0^T\int_\Gamma(q\boldsymbol{n})\cdot\boldsymbol{\varphi}\mathrm{d}S\mathrm{d}t=0
\end{aligned} \quad (38)$$

From the above equation, the terminal boundary condition can be obtained for the unsteady adjoint equation, where $\boldsymbol{\varphi}$ is a suitable test function

$$\int_\Omega\boldsymbol{\varphi}(T)\cdot\boldsymbol{\lambda}(T)\mathrm{d}V\mathrm{d}t=0 \quad (39)$$

This yields

$$\boldsymbol{\lambda}=0\quad\text{on }\Omega\times\{T\} \quad (40)$$

The velocity $\boldsymbol{u}$ is zero on boundaries $\Gamma_w\cup\Gamma_d$, while $\boldsymbol{u}\cdot\boldsymbol{n}$ is zero on the slip boundary. On the borders, the test functions are defined such that they vanish on the Dirichlet boundaries, i.e. $\boldsymbol{\varphi}=0$. The boundary conditions can hence be expressed as

$$\begin{aligned}
\boldsymbol{\lambda}&=0 \quad &&\text{on }\Gamma_{\text{in}}\cup\Gamma_w\cup\Gamma_d\times(0,T)\\
\nu\tfrac{\partial\boldsymbol{\lambda}}{\partial\boldsymbol{n}}-q\boldsymbol{n}&=\nu\tfrac{\partial\boldsymbol{u}}{\partial\boldsymbol{n}} \quad &&\text{on }\Gamma_{\text{out}}\times(0,T)
\end{aligned} \quad (41)$$

The partial derivative of $\mathcal{L}$ with respect to p evaluated with the function ϕ is given as

$$\left\langle\frac{\partial}{\partial p}\mathcal{L}(\Omega;\boldsymbol{\lambda},q,\boldsymbol{u},p);\phi\right\rangle=\int_0^T\int_\Omega\phi(\nabla\cdot\boldsymbol{\lambda})\mathrm{d}V\mathrm{d}t=0 \quad (42)$$

From equations (38)–(42), the strong form of the adjoint equation (22) can be derived.